


An *L*-Band Phased Array Radiometer for Sea Surface Salinity in Coastal Zones

Hailiang Lu , Hao Li, Yayun Cheng , *Member, IEEE*, Dong Zhu , *Member, IEEE*, Yinan Li, Pengju Dang, Rongchuan Lv, Rui Yu, and Yongjie Fu

Abstract—Sea surface salinity (SSS) in coastal zones with high temporal and spatial resolutions is also needed for scientific research and marine economy. However, one of the limitations of airborne *L*-band real-aperture microwave radiometers and synthesis aperture interferometric radiometers is high mass and volume or the high complexity of the system. To overcome the limitations, an *L*-band phased array radiometer is proposed as an alternative solution to monitor SSS in coastal zones from a small unmanned aerial vehicle (UAV). The *L*-band phased array radiometer is introduced, which only comprises a phased array and a single receiver. In addition, the calibration methods of the *L*-band phased array radiometer that the external calibration method and the internal calibration method, are also introduced. A series of experiments was performed to assess the performance of the *L*-band phased array radiometer. The results indicate that the *L*-band phased array radiometer show a good performance in low pointing angles and low scanning angles. As a conclusion, the *L*-band phased array radiometer can be an alternative solution to monitor SSS in coastal zones with high temporal and spatial resolutions from a small UAV.

Index Terms—Coastal zones, *L*-band, phased array, radiometer, sea surface salinity (SSS).

I. INTRODUCTION

SEA surface salinity (SSS) plays a fundamental role in the oceanography and climatology, which provides key information for investigating the ocean circulations and rainfall, and consequently for improving the estimates of seasonal to interannual climate predictions [1]. Currently, the global SSS can be remotely measured by means of two spaceborne *L*-band microwave radiometers: the European Space Agency's

Microwave Imaging Radiometer by Aperture Synthesis (MIRAS) in Soil Moisture and Ocean Salinity (SMOS) mission [2], [3], and the National Aeronautics and Space Administration's Aquarius instrument aboard the Argentinean spacecraft Satélite de Aplicaciones Científicas [4].

SMOS and Aquarius have achieved their scientific objectives in the open ocean with high SSS retrieval accuracy at the spatial resolutions (30–100 km and 150 km), respectively [5]. However, SSS in coastal zones from SMOS and Aquarius measurements is particularly challenging due to their coarse spatial resolution (30–100 km and 150 km) and/or land–sea contamination [6], [7]. In fact, high spatial and temporal resolution SSS in coastal zones is also required for scientific research and marine economy due to the high variation of SSS in coastal zones [8]–[10]. It is well known that SMOS and Aquarius from space are not adequate for SSS in coastal zones, where high spatial and temporal resolution SSS is demanded. However, *L*-band radiometers from airborne can fulfill the demand of SSS in coastal zones for high temporal and spatial resolutions, due to the low altitudes and without virtually any revisit time restrictions [11]. Since the small unmanned aerial vehicles (UAVs) have the advantages of high speed, convenience, and economy, the small UAVs can be used as a platform for *L*-band radiometers to map SSS in coastal zones. Meanwhile, the small UAVs at low altitudes ranging from hundreds of meters to a few kilometers can acquire spatial resolutions about tens of meters to hundreds of meters for *L*-band radiometer, and the revisit time can be adjusted as needed [8], [9]. However, the small UAVs have strict restrictions on the mass, volume, and complexity of *L*-band radiometer [11]. It is well known that the *L*-band real-aperture microwave radiometers from an airborne are high mass and volume due to bulk scanning platform, and the *L*-band synthesis aperture interferometric radiometer from an airborne without mechanical scanning is the high complexity of the system due to large antenna array [12]. To reduce the mass, volume, and complexity, the airborne *L*-band phased array radiometers have been developed with electronic scanning, not mechanical scanning, such as the scanning low frequency microwave radiometer [13] and PAU-RAD [14], [15].

To further reduce the mass, volume, and complexity, an *L*-band phased array radiometer is developed as a potential solution to monitor SSS in coastal zones for high temporal and spatial resolutions from a small UAV in this article. It employs an *L*-band phased array, not a bulk scanning platform, to simplify the hardware of the system and to reduce the mass, and volume of the system. It employs a single receiver to reduce the complexity

Manuscript received August 26, 2020; revised December 8, 2020; accepted December 13, 2020. Date of publication December 18, 2020; date of current version January 8, 2021. This work was supported in part by the National Natural Science Foundation of China under Grant 41706204 and Grant 61901244. (Corresponding author: Yayun Cheng.)

Hailiang Lu, Yinan Li, Pengju Dang, Rongchuan Lv, and Rui Yu are with the China Academy of Space Technology (Xi'an), Xi'an 710100, China (e-mail: hust_lhl@163.com; liyinan_cast@126.com; 651414063@qq.com; rosellinda_lrc@163.com; yur_cast504@163.com).

Hao Li is with the School of Electronics and Information Engineering, Beihang University, Beijing 100083, China, and also with the China Academy of Space Technology (Xi'an), Xi'an 710100, China (e-mail: cast504_lihao@163.com).

Yayun Cheng is with the Department of Engineering Physics, Tsinghua University, Beijing 100084, China (e-mail: chengyy915@163.com).

Dong Zhu is with the Department of Electronic Engineering, Tsinghua University, Beijing 100084, China (e-mail: zhudong_hust@163.com).

Yongjie Fu is with Wuhan Fingu Electronic Technology Company, Ltd., Wuhan 430200, China (e-mail: kaixinfyj@sohu.com).

Digital Object Identifier 10.1109/JSTARS.2020.3045813

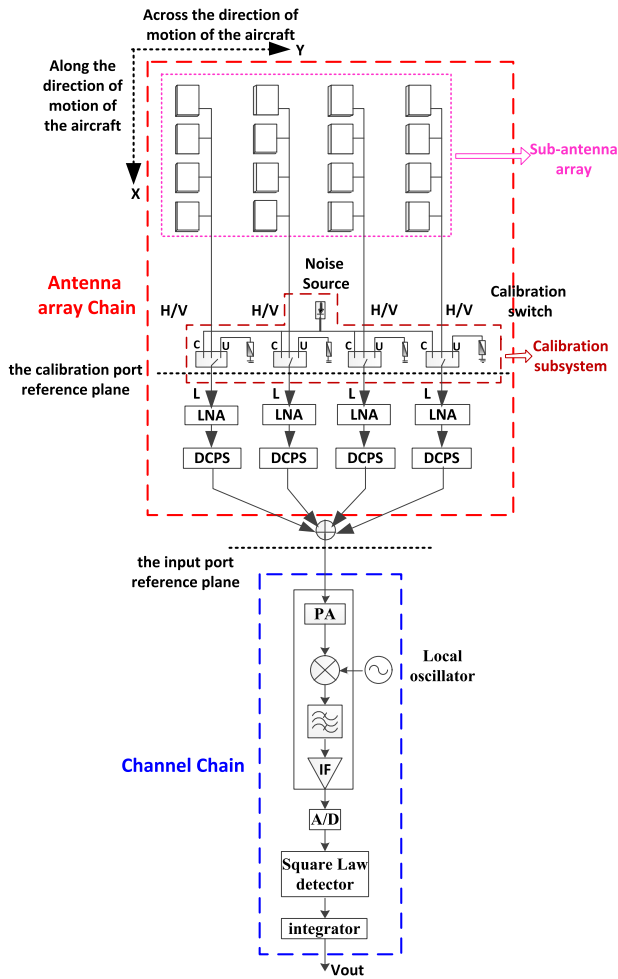


Fig. 1. Architecture sketch of the *L*-band phased array radiometer.

of the system. In addition, It can also measure the sea surface TB of the same scene in multiple incidence angles to improve SSS retrieved accuracy [16], [17]. This article is devoted to the *L*-band phased array radiometer with a phased array and a single receiver.

The rest of this article is organized as follows. The instrument that the *L*-band phased array radiometer is introduced in Section II. In Section III, the calibration methods are addressed, which comprise the internal calibration method and the external calibration method. The experiments are performed to assess the performance of the *L*-band phased array radiometer in Section IV. Finally, the conclusion is drawn and the further works are discussed in Section V.

II. L-BAND PHASED ARRAY RADIOMETER

This section is devoted to the architecture and key specifications of the *L*-band phased array radiometer. The architecture sketch of the *L*-band phased array radiometer is shown in Fig. 1, which comprises an antenna array chain and a channel chain. The phased array radiometer operates in the passive protected band 1400–1427 MHz with the vertical and horizontal polarizations. The center frequency is 1415 MHz and the bandwidth is

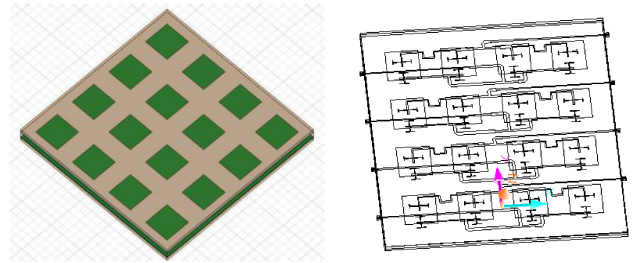


Fig. 2. (Left) Model of the *L*-band phased array antenna. (Right) The feed network of *L*-band phased array antenna.

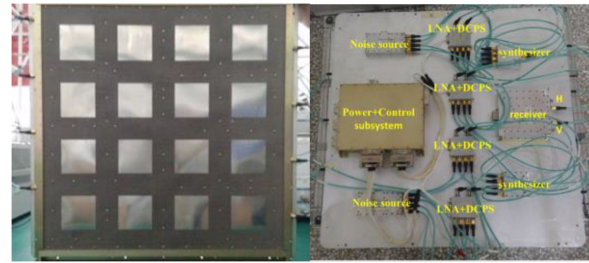


Fig. 3. *L*-band phased array radiometer. (Left) The *L*-band phased array antenna. (Right) The calibration subsystem and receiver.

20 MHz. The antenna array chain is formed by a 4×4 phased array antenna, a calibration subsystem, four low noise amplifiers (LNAs), four digital controlled phase shifters (DCPS), and a synthesizer. The phased array antenna is divided into four antenna subarrays, and each antenna subarray comprises four rectangular microstrip patch antennas and a feed network, as shown in Fig. 2. The calibration subsystem is formed by a noise source, a 1-4 power divider, four matched loads, and four calibration switches. In the antenna array chain, the LNAs are placed after each calibration switch due to preamplification resulting in improved gain and stability [18]. As shown in Fig. 1, the channel chain is a heterodyne microwave receiver, which is constituted by a power amplifier (PA), a mixer, a local oscillator, a low-pass filter, IF, A/D, a square law detector, and an integrator.

For the *L*-band phased array radiometer, the main beam efficiency (MBE) and the half-power beamwidth are two key specifications, which have a dependence on the adjacent element spacing and the antenna number of the phased array antenna. However, it is well known that the MBE degrades as the adjacent element spacing increases in a phased array antenna [16]. On the other hand, the half-power beamwidth increases as the adjacent element spacing increases in a phased array antenna [16]. Meanwhile, the antenna number of the phased array is limited by the airborne platform, especially for a small UAV. Although a high MBE and a high half-power beamwidth are expected in the *L*-band phased array radiometer, a compromise is made between the MBE and the half-power beamwidth for the phased array in the *L*-band radiometer, which has a dependence on the adjacent element spacing and the antenna number [16]. As a result, the designed phased array antenna is synthesized by 4×4 rectangular microstrip patch antennas with the adjacent element spacing 0.55λ along the x -axis and y -axis directions, as shown in Fig. 3 (left). The designed phased array antenna is

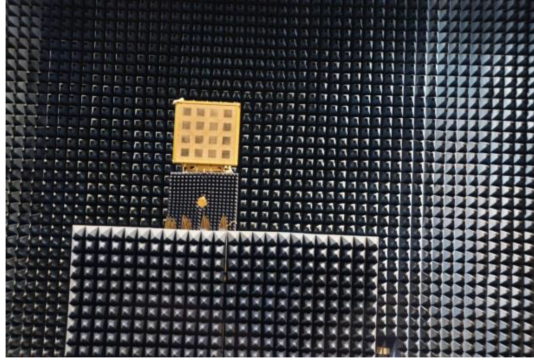


Fig. 4. Voltage patterns of the L-band phased array antenna are measured in a microwave anechoic chamber.

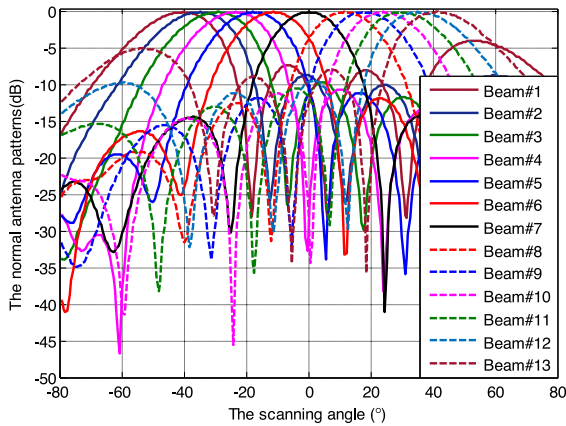


Fig. 5. Measured normalized antenna voltage pattern of Beam#1–Beam#13 in the vertical polarization.

analog combined along the direction of motion of the aircraft (the *x*-axis in Fig. 1), and the phased array antenna steers the beam up to $\pm 40^\circ$ from the bore-sight of the phased array, which has a half-power beamwidth lower than 25° (total 13 beams), across the direction of motion of the aircraft (the *y*-axis in Fig. 1). The MBE at bore-sight is expected to be larger than 90% in both directions.

The voltage patterns of Beam#1–Beam#13 of the L-band phased array antenna are measured in a microwave anechoic chamber, as shown in Fig. 4. The measured normalized antenna voltage patterns and MBE of Beam#1–Beam#13 in the vertical polarization are shown in Figs. 5 and 6, respectively. It can be seen that the MBE degrades as the scanning angle increases from nadir (Beam#7), especially in the outer scanning beams, as expected. That agrees well with the MBE characteristic of the phased array antennas [16]. It can also be seen that the MBE of Beam#4–Beam#10 is larger than 90%. As a result, the MBE degradation will reduce the performance of outer beams from nadir. The half-power beamwidth of Beam#1–Beam#13 in the vertical polarization is also shown in Fig. 7. It is found that half-power beamwidth also degrades as the scanning angle increases from nadir (Beam#7), as expected. The half-power beamwidth of Beam#4–Beam#10 is better than 25° . As shown in Figs. 6 and 7, it is found that the beams far from Beam #7 (Beam#1–Beam#3 and Beam#11–Beam#13) exhibit an obviously asymmetrical

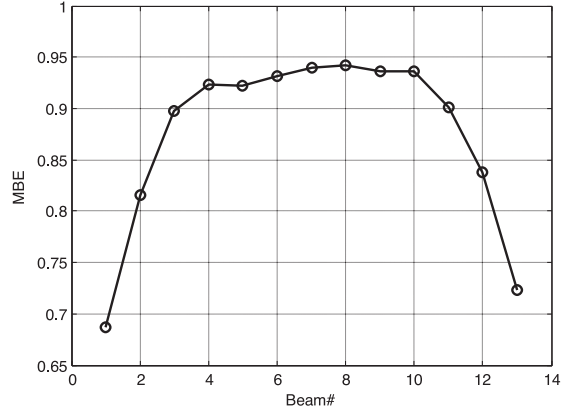


Fig. 6. MBE of Beam#1–Beam#13 in the vertical polarization.

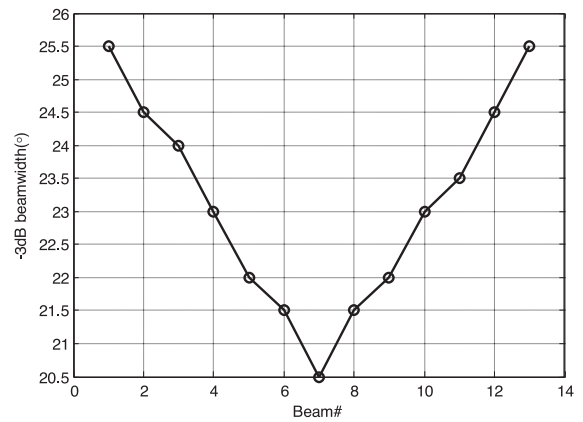


Fig. 7. -3 dB beamwidth of Beam#1–Beam#13 in the vertical polarization.

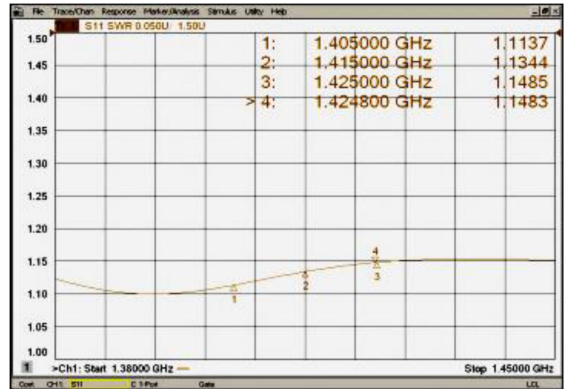


Fig. 8. VSWR of the L-band phased array antenna in the vertical polarization.

characteristic in the MBE and -3 dB beamwidth, which will reduce the performance of outer beams from nadir. The voltage standing wave ratio (VSWR) of the L-band phased array antenna in the vertical polarization is also shown in Fig. 8. The main specifications of the L-band phased array radiometer satisfy the designed requirements.

The calibration subsystem and the receiver are shown in Fig. 3 (right). In the calibration subsystem, two levels of correlated noises are generated by a common noise source, and uncorrelated noises are generated by the matched loads. The

correlated and uncorrelated noises are injected to the input ports of all LNAs, when the calibration switches are connected to the calibration ports (“C” port) and matched loads (“U” ports) in sequence (see Fig. 1). The internal calibration is performed to estimate the gain and offset of the system for each beam by driving correlated and uncorrelated noises to the input ports of all LNAs. When the phased array radiometer measures the sea surface TB, the calibration switches are connected to the antenna ports (“H” or “V” ports).

III. CALIBRATION METHODS

The section is devoted to the calibration methods for the L -band phased array radiometer, and two calibration methods are addressed that the internal calibration method and the external calibration method for the L -band phased array radiometer.

A. Internal Calibration Method

The internal calibration method is performed by driving correlated and uncorrelated noises to the input ports of all LNAs in the antenna array chain, which is similar to the centralized internal calibration method in MIRAS [19], [20], as shown in Fig. 1. Since the L -band phased array radiometer can be considered as a total power radiometer [21], the internal calibration method performed in the L -band phased array radiometer is relative simple by contrasting to MIRAS. In addition, since impedance mismatch and shifter losses vary with beam positions, separate calibrations are performed for each beam [22]. It also means that internal noises are injected to all the channels in each beam position.

In the internal calibration method, the antenna TB of four antenna subarrays is considered to be the same ($T_{a,i}^p = T_{a,j}^p = T_a$ ($i \neq j$)). In this case, the output voltage of receiver of one beam can be written as

$$\overline{V_{\text{out}}} = G \cdot \left(\left| \sum_{i=1}^4 (g_i \cdot w_i) \right| \cdot T_a + T_{\text{rec}} \right) \quad (1)$$

where G is the gain of the channel chain, T_{rec} denotes the total equivalent noise temperature generated by all elements of the L -band phased array radiometer in the input port reference plane of the channel chain (see Fig. 1), g_i is the gain of the i th antenna subarray chain, and w_i is the complex weight of the i th DCPS for one beam.

(1) can be also written as

$$\overline{V_{\text{out}}} = G_{\text{total}} \cdot T_a + T_{\text{off}} \quad (2)$$

where $G_{\text{total}} = G \cdot (|\sum_{i=1}^4 (g_i \cdot w_i)|)$ and $T_{\text{off}} = G \cdot T_{\text{rec}}$. It can be seen that the relationship between the antenna TB of the antenna subarrays and the output voltage of the radiometer is linear for each beam position. Thus, the common noise source and matched loads (see Fig. 1) with known temperatures are used to determine the calibration (2) of each beam position. In the internal calibration, the calibration switches are connected with the “C” ports (called “hot” source about 1100 K or “low” source about 320 K) and “U” ports (called “warm” source about 300 K) in sequence within each beam position, respectively. When the “hot” source and the “warm” source are injected into the

channel chain, the output voltages can be written as

$$\overline{V_{\text{out}}^{\text{hot}_i}} = G_{\text{total}}^i \cdot T_a^{\text{hot}} + T_{\text{off}}^i \quad (3)$$

$$\overline{V_{\text{out}}^{\text{warm}_i}} = G_{\text{total}}^i \cdot T_a^{\text{warm}} + T_{\text{off}}^i \quad (4)$$

where T_a^{hot} and T_a^{warm} denote the equivalent noise temperature of the “hot” source and “warm” source at the calibration switch output ports, respectively. Then, the total gain and offset in each beam position can be estimated as

$$G_{\text{total}}^i = \frac{\overline{V_{\text{out}}^{\text{hot}_i}} - \overline{V_{\text{out}}^{\text{warm}_i}}}{T_a^{\text{hot}} - T_a^{\text{warm}}} \quad (5)$$

$$T_{\text{off}}^i = \frac{T_a^{\text{warm}} * \overline{V_{\text{out}}^{\text{hot}_i}} - T_a^{\text{hot}} * \overline{V_{\text{out}}^{\text{warm}_i}}}{T_a^{\text{hot}} - T_a^{\text{warm}}} \quad (6)$$

Once the gain G_{total}^i and offset $T_{\text{off_set}}^i$ in each beam position are estimated, the scene TB can be estimated as

$$T_{\text{target}}^i = \frac{\overline{V_{\text{out}}^{\text{target}_i}} - T_{\text{off}}^i}{G_{\text{total}}^i} \quad (7)$$

where $\overline{V_{\text{out}}^{\text{target}_i}}$ denotes the output voltage of phased array radiometer of the i th beam. In addition, the physical temperatures of the matched loads must be kept to be the same and suppose that antenna temperature of each antenna subarray is also the same. Otherwise, the discrepancies within the physical temperatures of the matched loads and the antenna temperature of each antenna subarrays will slightly degrade the calibration accuracy. However, the accuracy knowledge of the physical temperature of the matched loads and the antenna subarrays will improve the calibration accuracy, the physical temperature can be accurately measured by the temperature sensors [23].

B. External Calibration Method

The external calibration method can also be considered as an alternative calibration method for the L -band phased array radiometer. The external calibration method is similar to the one point calibration method applied in SMOS [24], [25], which is performed by viewing the deep-sky (called “cold” source). In the external calibration method, the calibration switches are connected to the “A” (“H” or “V”) port and U-port in sequence for each beam position. In this case, the equivalent temperatures of the antenna subarrays and matched loads at the calibration switch output plane can be expressed as, respectively

$$T_a^{\text{cold}} = \eta_A T_{\text{sky}} |S_{LA}|^2 \quad (8)$$

$$T_a^{\text{warm}} = T_U \cdot |S_{LU}|^2 \quad (9)$$

where T_{sky} is the antenna TB of the L -band phased array antenna during deep-sky views, η_A denotes the antenna losses of the phased array antenna, which can be measured precisely on the ground and very stable all the time [19], T_U denotes the physical temperature of matched loads, S_{LA} and S_{LU} are the S -parameter between “L” port and “A” port or “U” port of the calibration switches, respectively, which are also accurately measured on the ground. Then, both (8) and (9) are substituted into (5) and (6) to estimate G_{total}^i and T_{off}^i . Since the physical temperature



Fig. 9. Field campaign of the *L*-band array phased radiometer in the open ocean. (Left) The vessel in the experimental ocean area. (Middle) The radiometer pointing toward the sky. (Right) The *L*-band phased array radiometer pointing toward the sea surface.

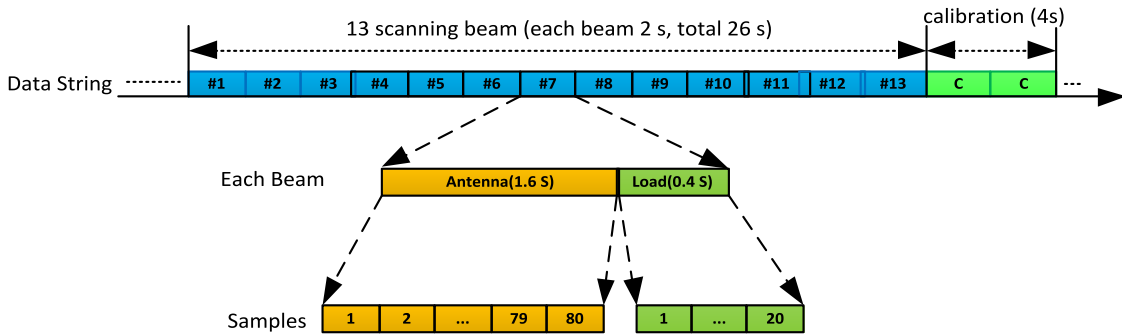


Fig. 10. Phased array radiometer timing diagram in the experiments.

of the phased array and the switches are kept to be the same, the equivalent noise temperature T_{off}^i generated by the antenna array chain and the channel chain at the calibration switch output plane is also the same [25].

Since the sea surface TB (about 100–200 K) at *L*-band is between the “warm” source (about 300 K) and the “cold” source (about 2.7–10 K), the calibration accuracy of the external calibration method is better than the calibration accuracy of the internal calibration method.

IV. EXPERIMENTS, RESULTS, AND DISCUSSIONS

To verify the performance of the *L*-band phased array radiometer, a series of experiments has been performed in the coastal zones close to the Dangan island, in Zhuhai City, China. In the experiments, the *L*-band phased array radiometer was installed on a ship, as shown in Fig. 9. To avoid the contribution of the Sun, the Sun is kept in the back-lobe of the *L*-band phased array radiometer.

In the experiments, the timing diagram of the *L*-band phased array radiometer is given in Fig. 10. As shown in Fig. 10, the *L*-band phased array radiometer steered from Beam#1 to Beam#13 in sequence and another individual calibration period was performed. The period of each scanning beam is 2 s, which is divided into the “target scene” (antenna) period with 1.6 s and the “warm” (matched loads) calibration period with 0.4 s. The individual calibration period is 4 s. As a result, the total period is $13 \times 2 \text{ s} + 4 \text{ s} = 30 \text{ s}$. The integrated time of the *L*-band phased array radiometer is 20 ms. The timing diagram and the

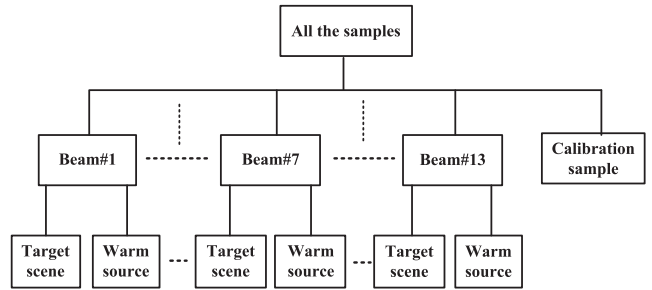


Fig. 11. Classification steps of the raw TB samples.

integrated time of the *L*-band phased array radiometer can also be adjusted as needed.

Since the *L*-band phased array radiometer was installed on a ship and the external calibration was easily performed with relatively high-calibration accuracy, the external calibration method (see Section III-B) was also performed in the experiments.

In the experiments, first, the deep-sky views were performed. Following that, the sea surface views were performed.

A. Deep-Sky Views

In the deep-sky views, the *L*-band phased array radiometer was performed to point toward the deep-sky [see Fig. 9 (middle)].

First, all voltage samples are classified into 13 beam sets and calibration sets (see Fig. 11) according to the timing diagram of all beams (see Fig. 10). As shown in Fig. 12, an example

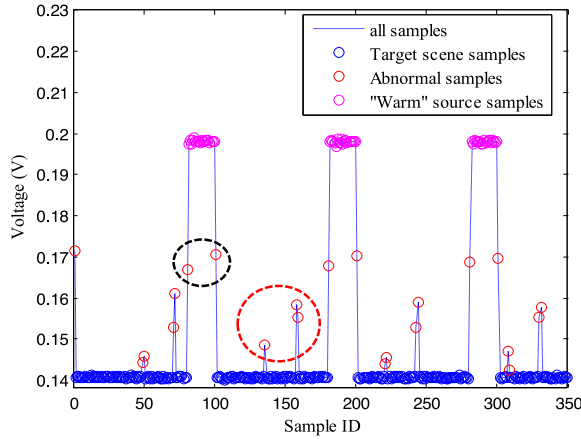


Fig. 12. Example of the voltage samples of classified Beam#7.

of the voltage samples of classified Beam#7 in the deep-sky views is given, which consists of the “target scene” subsets and the “warm” subsets. However, as shown in Fig. 12, it is found that there are some abnormal samples (small red circles) in the “target scene” subset. These abnormal samples are caused by the external radio frequency interference (RFI) sources (such as the samples in the large red dotted circle in Fig. 12) or the integral time between the “warm” calibration period and the “target scene” period (such as the samples in the large black dotted circle in Fig. 12). The abnormal samples caused by the external RFI sources in the “target scene” subsets can be detected and flagged by the proposed RFI detection algorithm in [26]. The abnormal samples caused by the integral time the “warm” calibration period and the “target scene” period can be easily identified and discarded due to these abnormal samples between the “target scene” samples and the “warm” samples in each beam.

Following that, according to Fig. 11, each beam set is classified into the “target scene” subset (the deep-sky in this section) and the “warm” subset (matched loads). The RFI detection algorithm in [26] was performed to flag the RFI contaminated samples in the “target scene” samples. Then, the “RFI-free” “target scene” samples and the “warm” samples of are obtained for each beam in the deep-sky views, which are used to perform the external calibration in the following section (see Section III-B). As shown in Fig. 13, the “RFI-free” “target scene” samples [Fig. 13(top)] and the “warm” samples [Fig. 13(bottom)] of Beam#1–Beam#13 in the deep-sky views are given. It is found that the “warm” samples associated matched loads are very stable. Further, it indicates that the receiver is stable, it also means that the gain (G_{total}^i) and offset ($T_{off_set}^i$) of each beam in the whole chain (7) are almost kept to be the same during a long time.

B. Sea Surface Views

In the sea surface views, the L-band phased array radiometer pointed toward the sea surface [see Fig. 9 (right)]. The scanning beam (β) was along horizontal direction. The pointing angle (α) that the angle between the normal line of the phased array and

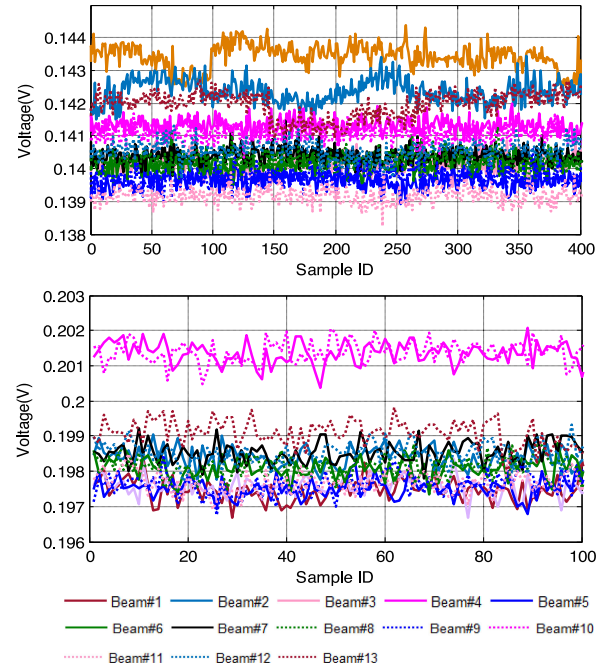


Fig. 13. “Target scene” “RFI-free” samples (top) and the “warm” samples (bottom) of Beam#1–Beam#13 during deep-sky views.

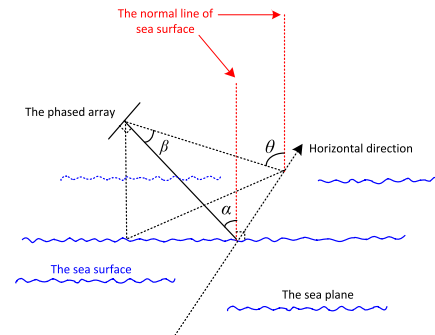


Fig. 14. Observation angle of the L-band phased array radiometer.

the normal line of the sea surface was changed sequentially as $\alpha = 33^\circ, 51^\circ, 67^\circ$, and 77° . As shown in Fig. 14, the incidence angle θ can be estimated as

$$\theta = \cos^{-1}(\cos(\alpha) * \cos(\beta)). \quad (10)$$

1) *Classification of the Raw TB Samples:* As the same process in the deep-sky views (see Section IV-A, Figs. 10 and 11), first, all voltage samples of the sea surface were also classified into 13 data beam sets and calibration sets. Then, each beam set was divided into the “target scene” subset and the “warm” subset. Finally, the “target scene” subsets and “warm” subsets of Beam#1–Beam#13 during the sea surface views are also classified according to the pointing angle α . The classification steps of the voltage samples have been shown in Fig. 9.

The “target scene” subsets of Beam#1–Beam#13 during the sea surface views are given in Fig. 15(a). As shown in Fig. 15(a), it is found that there are many abnormal samples within the red ellipses in the “target scene” subsets, which deviate too much from the neighboring samples, called strong RFI sources.

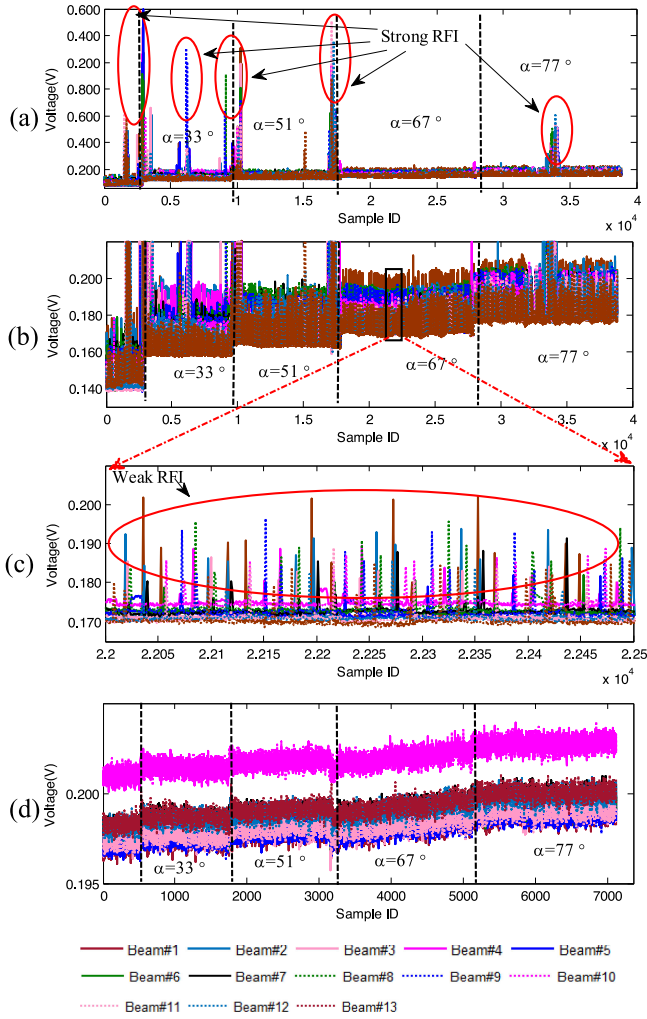


Fig. 15. (a) "Target scene" subsets of Beam#1–Beam#13 during sea surface views. (b) Zoom of Fig. 15(a). (c) Zoom of Fig. 15(b). (d) "warm" subsets of Beam#1–Beam#13 during sea surface views.

The zoom of Fig. 15(a) is given in Fig. 15(b). As shown in Fig. 15(b), it is also found that there are many weak abnormal samples in the "target scene" subsets. The zoom of Fig. 15(b) is given in Fig. 15(c). It is found that the weak abnormal samples are caused by pulsed interference signals. The "warm" subsets of Beam#1–Beam#13 during sea surface views are given in Fig. 15(d). However, there are no abnormal samples in the "warm" subsets [Figs. 13(b) and 15(d)]. The results also indicate that the abnormal samples are contaminated by external man-made RFIs, not caused by the L -band phased array radiometer. As shown in Fig. 15(d), the values of the "warm" subsets are almost consistent to that in the "warm" subsets during deep-sky views [see Fig. 13(b)]. The results also indicate that the L -band phased array radiometer is very stable, and the "RFI-free" "target scene" samples ("cold" source) and the "warm" samples ("warm" source) during the previous deep-sky views can be used as the "cold" source and "warm" source to estimate the gain (G_{total}^i) and offset ($T_{\text{off_set}}^i$) in (2) of each beam during the sea surface views.

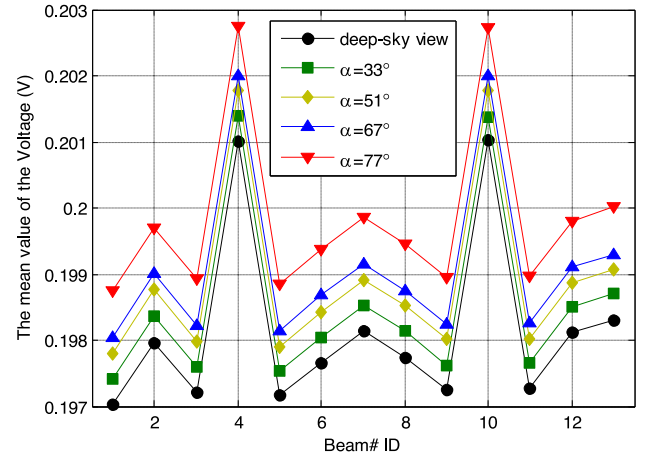


Fig. 16. Mean of the "warm" (matched loads) subsets of Beam#1–Beam#13 during the deep-sky views and sea surface views when $\alpha = 33^\circ$, 51° , 67° , and 77° .

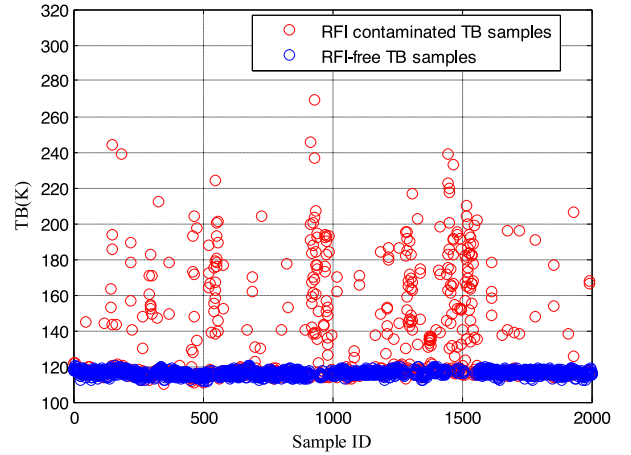


Fig. 17. Example of the RFI contaminated TB samples (red circles) and "RFI-free" TB samples (blue circles) of Beam#7 after performing the RFI detection algorithm.

The mean of the "warm" subset of Beam#1–Beam#13 during the sea surface views is given in Fig. 16. In the ideal case, the mean of the "warm" subset of Beam#1–Beam#13 should be the same in different pointing angles (α). However, it is found that the "warm" mean of Beam#1–Beam#13 slightly increases as the pointing angle (α) (incidence angle) increases. In the experiments, the L -band phased array radiometer operated at V polarization, and the antenna TB of each beam in V polarization during the sea surface views increases as the pointing angle (incidence angle) increases. That may be caused by the coupling effect (poor isolation) between the "V" ports and "L" ports of the calibration switches. When the calibration switches are connected to the "U" ports, the equivalent coupling noise temperature from the "V" ports to the "L" ports (see Fig. 1) increases as the antenna TB increases, which increases as the pointing angle increases (the incidence angle). Thus, the isolation of the calibration switches should be improved to mitigate the coupling effects. In addition, it is also found that the "warm" subset mean

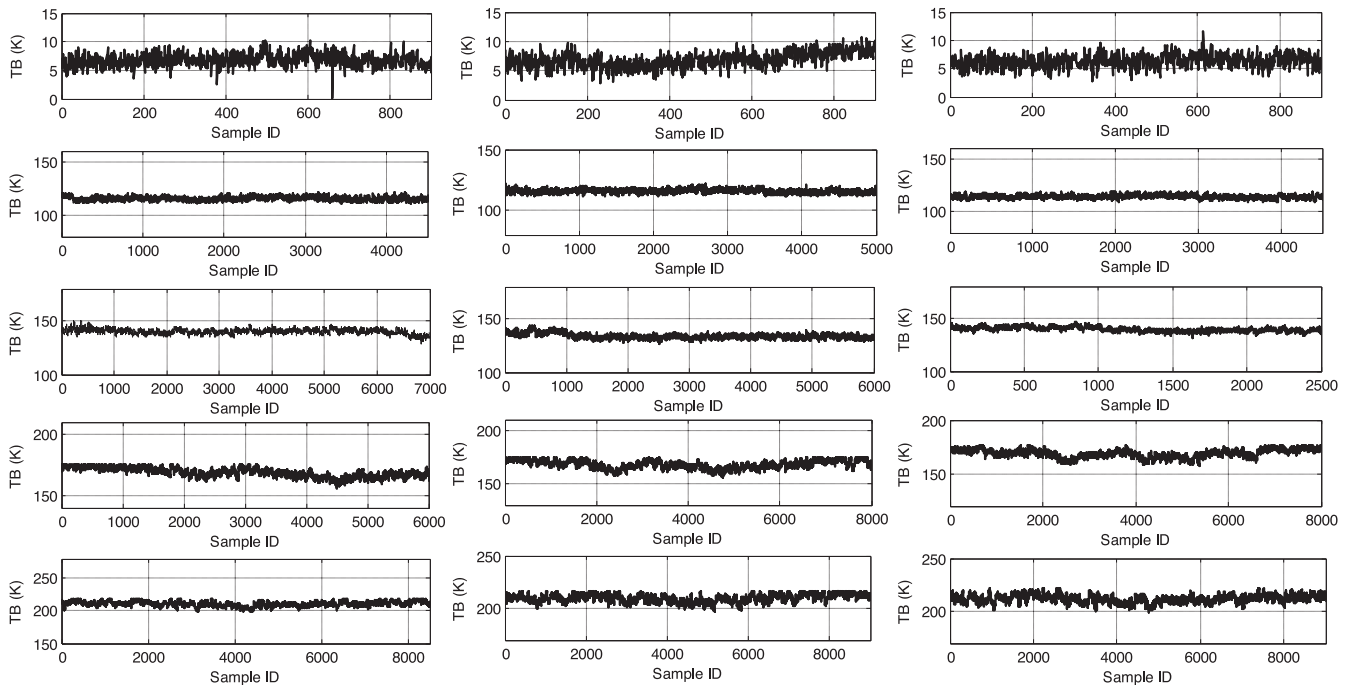


Fig. 18. “RFI-free” TB samples of Beam#6(left), Beam#7 (middle), and Beam#8 (right) when $\alpha = 180^\circ$ (deep-sky), 33° , 51° , 67° , and 77° (from top to bottom), respectively.

also varies as the different scanning angles (different beam), that may be due to the gain (G_{total}^i) of each beam is slightly different caused by pulsed interference signals.

2) *Sea Surface TB as a Function of the Incidence Angle:* After the classification of the samples, the RFI detection algorithm in [26] is performed to flag RFI contaminated voltage samples and obtain the “RFI-free” voltage samples. After that, the external calibration (see Section III-A) is performed, in which the “cold” source and the “warm” source provided by deep-sky views are used (see Section IV-A). Then, the “raw” TB samples and “RFI-free” TB samples of each beam are obtained. For example, the RFI contaminated TB samples (red circles) and “RFI-free” TB samples (blue circles) of Beam#7 are given in Fig. 17, respectively. It indicates that the RFI detection algorithm can effectively flag most RFI contaminated TB samples. In addition, the contributions of the galactic reflected radiation and the upwelling reflected radiation of atmosphere were considered and removed. In the experiments, the contribution of the galactic reflected radiation is about 6 K and the contribution of the upwelling reflected radiation is about 2.4–2.8 K [27], [28]. Finally, the “RFI-free” TB samples of the sea surface are obtained. As an example, the “RFI-free” TB samples of Beam#6, Beam#7, and Beam#8 are given in Fig. 18 when $\alpha = 180^\circ$ (deep-sky), 33° , 51° , 67° , and 77° (from top to bottom), respectively.

The mean of “RFI-free” TB samples of Beam#1–Beam#13 during the sea surface views is shown in Fig. 19, when $\alpha = 33^\circ$, 51° , 67° , and 77° . In addition, the simulated TB sample in V-polarization as a function of the incidence angle is also shown in Fig. 19, predicted by the Klein and Swift model [29] based on the *in situ* parameters measured in the experiments.

As shown in Fig. 19, it is found that the mean of “RFI-free” TB samples as a function of the incidence angle shows a good agreement with the theoretical simulated TB curve in the low pointing angles ($\alpha = 33^\circ$ and 51°) and low scanning angle (Beam#6–Beam#8), using the realistic conditions. It indicates that the radiometer exhibits a good performance in low incidence angles and the inner scanning beams from nadir (Beam#7). However, it is found that the mean of “RFI-free” TB samples in large pointing angles ($\alpha = 67^\circ$ and 77°) and middle scanning angles (Beam#4–Beam#5 and Beam#9–Beam#10) is lower than that in the theoretical simulated TB curve. That is due to more side lobes pointing to the sky in large pointing angles ($\alpha = 67^\circ$ and 77°) [30]. As shown in Fig. 20, the normalized antenna voltage pattern of Beam#7 is given in different pointing angles $\alpha = 33^\circ$, 51° , 67° , and 77° . It is found that more side lobes point to the sky in large pointing angles, as expected. However, the L-band phased array radiometer will exhibit a better performance from airborne, because of less sidelobes pointing to the sky, as shown in Fig. 21. In addition, it is also found that the mean of “RFI-free” TB samples large scanning angles (Beam#1–Beam#3 and Beam#11–Beam#13) is far lower than that in the theoretical simulated TB curve. That may be not only caused by more side lobes pointing to the sky in large scanning angles and the low MBE in the large scanning angle, but also caused by the seriously asymmetrical characteristic in the large scanning angles (Beam#1–Beam#3 and Beam#11–Beam#13), as mentioned in Section II.

In Fig. 19, it is also found that the mean of “RFI-free” TB samples in large scanning angle (β) is lower than that in the theoretical simulated curve in the same pointing angle, which is

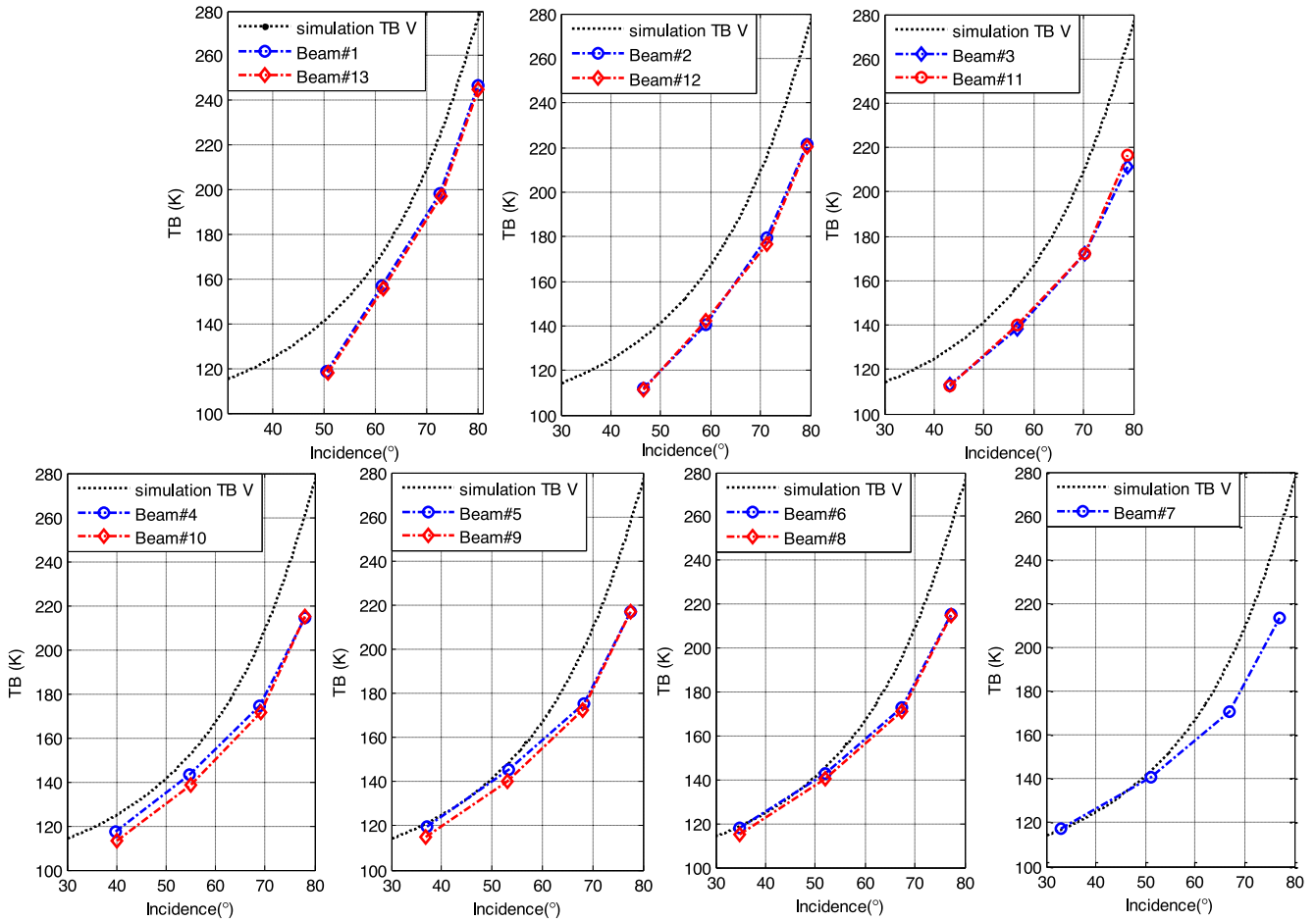


Fig. 19. Simulated TBs as a function of the incidence angle, and the mean of the “RFI-free” TB samples of Beam#1–Beam#13 when $\alpha = 33^\circ$ (a), 51° (b), 67° (c), and 77° (d), respectively.

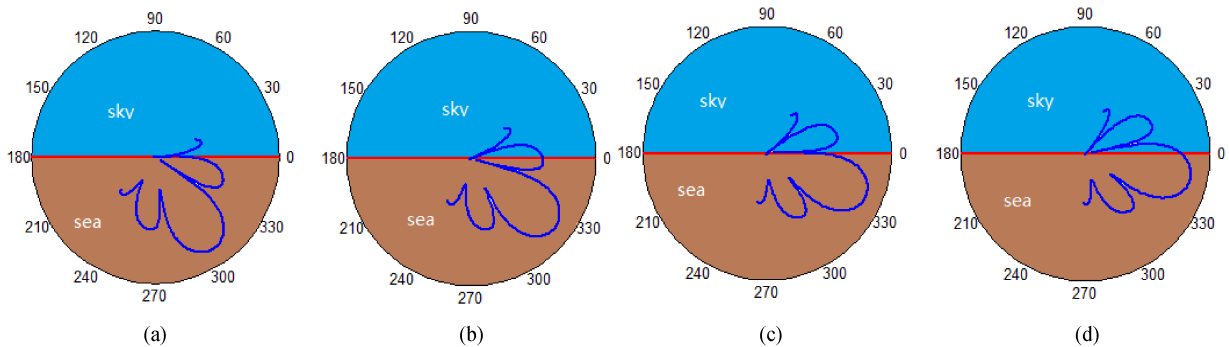


Fig. 20. Normalized antenna voltage pattern of Beam#7 points toward to sea surface in different pointing angles $\alpha = 33^\circ$ (a), 51° (b), 67° (c), and 77° (d), respectively.

also due to more side lobes pointing to the sky in large scanning angles and the low MBE in the large scanning angle (β). It indicates that the performance of the phased array radiometer degrades as the scanning angle increases, as expected.

C. Sea Surface Salinity

In the experiments, SSS in the flied campaign is about 32 psu measured by a CTD. SSS is retrieved by the “RFI-free” TB

samples of Beam#6–Beam#8, using the Klein and Swift model [29]. The root mean square (RMS) between the retrieved SSS of Beam#6–Beam#8 and the measured SSS of the CTD is shown in Table I, when $\alpha = 33^\circ, 51^\circ, 67^\circ,$ and 77° . As shown in the table, it is found that the RMS between the retrieved SSS of Beam#6–Beam#8 and the measured SSS of the CTD increases as the incidence angle increases. That may be due to the reduced performance of the *L*-band phased array radiometer in large incidence angle for each beam. In addition, it is also found

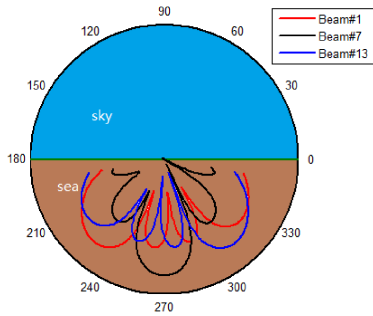


Fig. 21. Sketch map of Beam#1, Beam#7, and Beam#13 of the *L*-band phased array radiometer from airborne.

TABLE I
RETRIEVED SSS BY BEAM#6–BEAM#8 AND THE MEASURED SSS BY THE CTD

Beam	Incidence(°)	RMS (PSU)	CTD (PSU)
Beam#6	34.7	2.4	32
	51.9	2.9	32
	67.5	4.8	32
	77.3	4.7	32
Beam#7	33.0	1.7	32
	51.0	1.8	32
	67.0	5.1	32
	77.0	5.9	32
Beam#8	34.7	1.8	32
	51.9	3.4	32
	67.5	6.9	32
	77.3	5.1	32

that the RMS between the retrieved SSS of Beam#6–Beam#8 and the measured SSS of the CTD increases the scanning angle increases from nadir (Beam#7). That is also due to the reduced performance of the *L*-band phased array radiometer in large scanning angles, which is caused by the reduced MBE in large scanning angles in the *L*-band phased array.

V. CONCLUSION

In this article, an *L*-band phased array radiometer is developed to monitor SSS in coastal zones with high temporal and spatial resolution from a small UAV, which only comprises a phased array and a single receiver to reduce the mass and volume of *L*-band radiometer and simplify the hardware of the system. The calibration methods, that the internal and external calibration method, are also introduced. A series of experiments was also performed to assess the performance of the *L*-band phased array radiometer in terms of the deep-sky views and the sea surface views. The results indicate that the *L*-band phased array radiometer exhibits a good performance in low incidence angle and low scanning beams from nadir (Beam#7). However, the mean of the “RFI-free” TB samples in large pointing angle or large scanning angles is lower than that in the theoretical simulated curve, which may be due to more cold sky entering the sidelobes and/or main beams in large pointing angles, the low MBE and/or seriously asymmetrical characteristic in large scanning angles. In addition, the retrieved SSS by Beam#6–Beam#8 is also analyzed and discussed. It is found that the RMS between the retrieved SSS by

Beam#6–Beam#8 and the measured SSS by the CTD increases as the incidence angle or the scanning angle increases. That also may be due to the reduced performance of the *L*-band phased array radiometer in large incidence angle, the reduced MBE and seriously asymmetrical characteristic in large scanning angles.

In future work, the MBE can be improved by increasing the number of the antenna elements in the phased array to improve the performance of the *L*-band phased array radiometer in large scanning angles. As a conclusion, the *L*-band phased array radiometer can be an alternative solution from a small UAV to monitor SSS.

ACKNOWLEDGMENT

The authors would like to thank the anonymous reviewers for their valuable comments and suggestions, which help them to improve the quality of the article.

REFERENCES

- [1] G. S. E. Lagerloef, “Introduction to the special section: The role of surface salinity on upper ocean dynamics, air-sea interaction and climate,” *J. Geophys. Res.*, vol. 107, no. C12, pp. SRF 1-1–SRF 1-2, 2002.
- [2] P. Silvestrin, M. Berger, Y. Kerr, and J. Font, “ESA’s second Earth Explorer opportunity mission: The Soil Moisture and Ocean Salinity mission—SMOS,” *IEEE Geosci. Remote Sens. Newslett.*, vol. 118, pp. 11–14, Mar. 2001.
- [3] X. Yin, J. Boutin, and P. Spurgeon, “First assessment of SMOS data over open ocean: Part I—Pacific Ocean,” *IEEE Trans. Geosci. Remote Sens.*, vol. 50, no. 5, pp. 1648–1661, May 2012.
- [4] D. M. Le Vine, G. S. E. Lagerloef, F. R. Colomb, S. H. Yueh, and F. A. Pellerano, “Aquarius: An instrument to monitor sea surface salinity from space,” *IEEE Trans. Geosci. Remote Sens.*, vol. 45, no. 7, pp. 2040–2050, Jul. 2007.
- [5] J. Boutin *et al.*, “New SMOS sea surface salinity with reduced systematic errors and improved variability,” *Remote Sens. Environ.*, vol. 214, pp. 115–134, Sep. 2018.
- [6] I. Corbella *et al.*, “Impact of correlator efficiency errors on SMOS land–sea contamination,” *IEEE Trans. Geosci. Remote Sens. Lett.*, vol. 12, no. 9, pp. 1813–1817, May 2015.
- [7] Y. Li, Q. Li, and H. Lu, “Land contamination analysis of SMOS brightness temperature error near coastal areas,” *IEEE Trans. Geosci. Remote Sens. Lett.*, vol. 14, no. 5, pp. 587–591, Mar. 2017.
- [8] E. M. McIntyre and A. J. Gasiewski, “An ultra-lightweight *L*-band digital lobe-differencing correlation radiometer (LDCR) for airborne UAV SSS mapping,” in *Proc. IEEE Int. Geosci. Remote Sens. Symp.*, Barcelona, Spain, 2007, pp. 1095–1097.
- [9] R. Acevo-Herrera, A. Aguasca, X. Bosch-Lluis, and A. Camps, “On the use of compact *L*-band Dicke radiometer (ARIEL) and UAV for soil moisture and salinity map retrieval: 2008/2009 field experiments,” in *Proc. IEEE Int. Geosci. Remote Sens. Symp.*, Cape Town, South Africa, 2009, pp. 729–732.
- [10] R. A. Vandermeulen, R. Arnone, S. Ladner, and P. Martinolich, “Estimating sea surface salinity in coastal waters of the Gulf of Mexico using visible channels on SNPP-VIIRS,” *Proc. SPIE*, vol. 9111, May 2014, Art. no. 911109.
- [11] R. Acevo-Herrera *et al.*, “Design and first results of an UAV-borne *L*-band radiometer for multiple monitoring purposes,” *Remote Sens.*, vol. 2, no. 7, pp. 1662–1679, Jun. 2010.
- [12] H. Lu *et al.*, “A hybrid calibration method for aperture synthesis radiometers,” *IEEE Geosci. Remote Sens. Lett.*, vol. 13, no. 5, pp. 651–655, Mar. 2016.
- [13] A. Prytz, M. L. Heron, D. M. Bunaget, and M. Goodberlett, “Calibration of scanning low frequency microwave radiometer,” in *Proc. OCEANS MTS/IEEE*, Oct. 2002, pp. 2003–2007.
- [14] A. Camps, X. Bosch-Lluis, I. Ramos-Perez, J. F. Marchan, B. Izquierdo, and N. Rodriguez, “New instrument concepts for ocean sensing: Analysis of the PAU radiometer,” *IEEE Trans. Geosci. Remote Sens.*, vol. 45, no. 10, pp. 3180–3192, Oct. 2007.

- [15] X. Bosch-Lluis, A. Camps, I. Ramos-Perez, J. F. Marchan-Hernandez, N. Rodriguez-Alvarez, and E. Valencia, "PAU/RAD: Design and preliminary calibration results of a new L-band pseudo-correlation radiometer concept," *Sensors*, vol. 8, no. 7, pp. 4392–4412, Jul. 2008.
- [16] X. Bosch-Lluis, I. Ramos-Perez, A. Camps, N. Rodriguez-Alvarez, E. Valencia, and J. F. Marchan-Hernandez, "Description and performance of an L-band radiometer with digital beam-forming," *Remote Sens.*, vol. 3, no. 1, pp. 14–40, Dec. 2011.
- [17] C. Swift and R. E. McIntosh, "Considerations for microwave remote sensing of ocean surface salinity," *IEEE Trans. Geosci. Remote Sens.*, vol. GRS-21, no. 4, pp. 480–491, Oct. 1983.
- [18] M. K. Sonmez, R. J. Trew, and C. P. Hearn, "Front-end topologies for phased array radiometry," in *Proc. Eur. Microw. Conf.*, Helsinki, Finland, 1992, pp. 1251–1256.
- [19] A. J. Camps Carmona, "Application of interferometric radiometry to earth observation," Ph.D. dissertation, Dept. Telecommun. Eng., Universitat Politècnica de Catalunya, Barcelona, Spain, 1996.
- [20] F. Torres, A. Camps, J. Bara, and I. Corbella, "On-board phase and modulus calibration of large aperture synthesis radiometers study applied to MIRAS," *IEEE Trans. Geosci. Remote Sens.*, vol. 34, no. 4, pp. 1000–1009, Jul. 1996.
- [21] H. Lu, Y. Li, R. Yu, A. Jin, and R. Lv, "A L-band phased array radiometer for sea surface salinity," in *Proc. IEEE Int. Geosci. Remote Sens. Symp.*, Fort Worth, TX, USA, 2017, pp. 2935–2938.
- [22] H. K. Schuman, "Phased array antenna design considerations for large aperture microwave radiometer earth observations," in *Proc. IEEE Antennas Propag. Soc. Int. Symp.*, Ann Arbor, MI, USA, 1993, pp. 720–723.
- [23] S. Vedrilla, "Calibration, validation and polarimetry in 2D aperture synthesis: Application to MIRAS," Ph.D. dissertation, Dept. Telecommun. Eng., Universitat Politècnica de Catalunya, Barcelona, Spain, 2005.
- [24] J. Lemmetyinen *et al.*, "SMOS calibration subsystem," *IEEE Trans. Geosci. Remote Sens.*, vol. 45, no. 11, pp. 3691–3700, Nov. 2007.
- [25] F. Torres *et al.*, "Denormalization of visibilities for in-orbit calibration of interferometric radiometers," *IEEE Trans. Geosci. Remote Sens.*, vol. 44, no. 10, pp. 2679–2686, Oct. 2006.
- [26] H. Lu *et al.*, "An RFI detection and mitigation algorithm for an L-band phased array radiometer," *IEEE Geosci. Remote Sens. Lett.*, vol. 17, no. 5, pp. 779–783, May 2020.
- [27] S. H. Yueh, R. West, W. J. Wilson, F. K. Li, E. G. Njoku, and Y. Rahmat-Samii, "Error sources and feasibility for microwave remote sensing of ocean surface salinity," *IEEE Trans. Geosci. Remote Sens.*, vol. 39, no. 5, pp. 1049–1059, May 2001.
- [28] J. Font, M. Talone, M. Portabella, and C. Gabarro, "Toward an optimal SMOS ocean salinity inversion algorithm," *IEEE Geosci. Remote Sens. Lett.*, vol. 6, no. 3, pp. 509–513, Jul. 2009.
- [29] L. A. Klein and C. T. Swift, "An improved model for the dielectric constant of sea water at microwave frequencies," *IEEE Trans. Antennas Propag.*, vol. AP-25, no. 1, pp. 104–111, Jan. 1977.
- [30] X. Bosch-Lluis, "On the design of microwave radiometers with digital beamforming and polarization synthesis for earth observation," Ph.D. dissertation, Dept. Telecommun. Eng., Universitat Politècnica de Catalunya, Barcelona, Spain, 2011.



Hailiang Lu received the B.S. degree in electrical engineering from China Three Gorges University, Yichang, China, in 2009, the M.S. degree in the electromagnetic field and microwave technology from Guilin University of Electronic Technology, Guilin, China, in 2012, the Ph.D. degree in the electromagnetic field and microwave technology from Huazhong University of Science and Technology, Wuhan, China, in 2016.

He is currently a Senior Engineer with the China Academy of Space Technology (Xi'an), Xi'an, China.

His research interests include the passive microwave remote sensing, the passive microwave detection, and the radio frequency interference detection.



Hao Li received the B.S. degree in electrical engineering from Xidian University, Xi'an, China, in 2002, and the M.S. degree in electronic engineering from the China Academy of Space Technology, Xi'an, China, in 2005. He is currently working toward the Ph.D. degree in electronic and information engineering with Beihang University, Beijing, China.

He is a Professor with the China Academy of Space Technology (Xi'an). His research interests include the passive microwave remote sensing and the microwave radiometer design.



Yayun Cheng (Member, IEEE) was born in Anhui, China, in 1990. He received the B.S. degree in applied physics from Hefei University of Technology, Hefei, China, in 2012, and the Ph.D. degree in electronic engineering from Huazhong University of Science and Technology, Wuhan, China, in 2018.

He is currently a Postdoctoral Fellow with the Department of Engineering Physics, Tsinghua University, Beijing, China, and with the National Engineering Laboratory for Dangerous Articles and Explosives Detection Technologies, Beijing, China, since

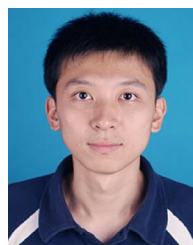
2019. His research interests include microwave remote sensing, millimeter-wave and terahertz imaging, polarization imaging, multisource image processing, and physically based information extraction.

Dr. Cheng was the recipient of the Excellent Doctoral Dissertation Award of China Education Society of Electronics, in 2019.



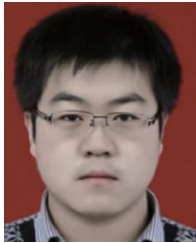
Dong Zhu (Member, IEEE) received the B.S. degree in communication engineering and Ph.D. degree in electronic science and technology from Huazhong University of Science and Technology, Wuhan, China, in 2013 and 2018, respectively.

He is currently a Postdoctoral Fellow with the Department of Electronic Engineering, Tsinghua University, Beijing, China. His research interests include antenna arrays, array signal processing, microwave remote sensing, and numerical optimization techniques for electromagnetic problems.



Yinan Li received the B.S. and M.S. degrees in electrical engineering from Xidian University, Xi'an, China, in 2007 and 2010, respectively.

He is currently a Senior Engineer with the China Academy of Space Technology (Xi'an), Xi'an, China. His research interests include passive microwave remote sensing and microwave radiometer design.



Pengju Dang received the B.S. degree in electrical engineering from Xidian University, Xi'an, China, in 2010, and the M.S. degree in electronic engineering from the China Academy of Space Technology, Xi'an, China, in 2013.

He is currently an Engineer with the China Academy of Space Technology (Xi'an). His research interests include microwave remote sensing, radiometer system design, and system calibration.



Rui Yu received the B.S. degree in electrical engineering from Chang'an University, Xi'an, China, in 2006, and the M.S. degree in electrical engineering from Xidian University, Xi'an, China, in 2009.

He is currently a Senior Engineer with the China Academy of Space Technology (Xi'an), Xi'an, China. His research interests include the passive microwave remote sensing and the microwave radiometer design.



Rongchuan Lv received the B.S. and M.S. degrees in electrical engineering from Xidian University, Xi'an, China, in 2004 and 2007, respectively.

She is currently a Professor with the China Academy of Space Technology (Xi'an), Xi'an, China. Her research interests include the passive microwave remote sensing and the microwave radiometer design.



Yongjie Fu received the B.S. degree in information display and photoelectric technology from the University of Electronic Science and Technology of China, Chengdu, China, in 2007, and the M.S. degree in electromagnetic field and microwave technology from Guilin University of Electronic Technology, Guilin, China, in 2012.

He is currently an Engineer with the Wuhan Fingu Electronic Technology Company, Ltd., Wuhan, China. His research interests include engineering electromagnetism and phased array.